An Online Tool Temperature Monitoring Method based on Physics-guided Infrared Image Features and Artificial Neural Network for Dry Cutting

Kok-Meng Lee*, *Fellow*, *IEEE*, Yang Huang, Jingjing Ji*, *Member*, *IEEE*, and Chun-Yeon Lin

***Abstract*— The paper presents an efficient method, which reconstructs the temperature field around the tool/chip interface from infrared (IR) thermal images, for online monitoring the internal peak temperature of the cutting tool. The tool temperature field is divided into two regions; namely, a far field for solving the heat-transfer coefficient between the tool and ambient temperature, and a near field where an artificial neural network (ANN) is trained to account for the unknown heat variations at the frictional contact interface. Methods to extract physics-based feature points from the IR image as ANN inputs are discussed. The effects of image resolution, feature selection, chip occlusion, contact heat variation and measurement noises on the estimated contact temperature are analyzed numerically and experimentally. The proposed method has been verified by comparing the ANN-estimated surface temperatures against "true values" experimentally obtained using a high-resolution IR imager on a custom-designed testbed as well as numerically simulated using finite-element analysis. The concept feasibility of the temperature monitoring method is demonstrated on an industrial lathe-turning center with a commercial tool insert.**

***Note to Practitioners* —The internal tool-temperature field around the tool/chip interface during cutting offers essential information to monitor tool-wear and ensure surface-quality particularly in finishing cuts, which is difficult to be monitored because of the stringent real-time requirements (including low cost and high accuracy) in harsh working environments. This paper presents a potentially low-cost solution that combines non-contact surface temperature measurements with high-fidelity physics-based computational models for monitoring the internal peak temperature at the tool/chip frictional contact during cutting. This physics-based method requires only a small number of pre-selected features, and uses thermal isotherms and streamlines to detect and substitute any occlusions in the IR images. The method does not rely on high-resolution images to infer the steep temperature gradient near the tool-tip where the peak temperature occurs, and thus can be implemented with a relatively low-cost IR imager. Unlike traditional least-square methods that bases solutions to a heat-conduction partial differential equation (PDE), the ANN is trained with precomputed physics-based models based on a novel dual-field (far-field and near-field) approach. The ANN-based method not only eliminates the need to solve the time-demanding PDE in real time, but also effectively accounts for parameter variations due to the uncertain frictional heat-fluxes at the contact interface during cutting.**

***Index Terms* — online monitoring, infrared (IR) imaging, temperature measurements, artificial neural network (ANN), thermal field reconstruction, manufacturing, machining.**

I. Introduction

RAPID advancements in imaging/computing technologies [1] and machine intelligence [2] have motivated manufacturers to develop online sensing methods to maintain product quality with improved production rate [3][4], particularly for monitoring tool wear and controlling the dynamic behaviors in fabricating thin-walled aircraft components which are generally made of hard-to-machine materials (such as titanium alloy) that typically have a low heat conductivity. Among the challenges is the online measurement of the internal tool-temperature field and its peak value of the cutting tool subject to unknown contact heat variations, which are essential information to monitor tool-wear behaviors, prevent premature tool-failure, and ensure surface quality particularly in finishing cuts. As the contact temperature and its steep gradient along with the unpredictable contact heat variations cannot be directly measured [2], existing methods to predict tool wear are empirical and rely on operationally expensive pre-scheduled tool-changes. There is a need for an online monitoring method capable of reconstructing the internal temperature field around the tool/chip interface from high-fidelity models with non-contact surface measurements while the component is being fabricated.

Existing methods that determine the heat exchange at the micro-scale contact area can be broadly divided into three categories: *Experimental* techniques with embedded thermocouples (TCs) focus on direct measurements of the cutting tool temperatures. Predictive *theoretical* models aim at understanding the physical phenomena to improve or optimize the cutting process. *Hybrid* experimental/ numerical inverse heat-conduction methods estimate the boundary conditions at the contact interface. To gain physical insights into thermal effects on tool wear, several direct- measurement methods have been explored. Based primarily on conventional thermocouples (TCs) [6][7] and recently developed thin-film TCs (TFTCs) [8][9] that take advantages of MEMS technology, an embedded or surface-mounted TCs/TFTCs was integrated in a cutting tool as micro-scale sensors to monitor the tool temperature near the

This work was supported in part by the National Natural Science Foundation of China (Grant No.51505168), U. S. National Science Foundation (CMMI-1662700), National Basic Research Program of China (973 Program, Grant No.2013CB035803).

Kok-Meng Lee, Yang Huang and Jingjing Ji are with the State Key Lab. of Dig. Manuf. and Equip. Tech. (SKL-DMET), and Sch. of Mech. Sci. and Eng. at Huazhong Univ. of Sci. and Tech. (HUST), Wuhan, Hubei, 430074, P. R. China. Kok-Meng Lee is also with the George W. Woodruff Sch. of Mech. Eng. at Georgia Inst. of Tech., Atlanta, GA 30332-0405 USA.

Chun-Yeon Lin is with the George W. Woodruff School of Mech. Eng. at Georgia Inst. of Tech., Atlanta, GA 30332 USA.

* *Corresponding author: Kok-Meng Lee* (kokmeng.lee@me.gatech.edu) and *Jingjing Ji* (jijingjing@hust.edu.cn).

tool/chip interface during cutting. Experimentally measured temperature (up to 900°C) at a distance of 0.2mm from the tool tip was reported [10]. Predictive theoretical models [11] are of great interest for assessing the temperature field at the tool/chip interface; such models often rely on assumptions to estimate parameters and experiments to validate calculations. Hybrid methods generally use an inverse technique to determine the boundary conditions numerically with temperature measurements at specified points in the tool, and then solve the heat conduction equation for the internal temperature at the tool/chip interface. Most existing inverse methods generally base on a least-square formulation that numerically solves the 3D partial differential equation (PDE) using finite element [12] or finite difference [13] techniques, which are computationally demanding for real-time applications. These (experimental, theoretical and hybrid) methods more or less involve experimental measurements typically with TCs, more recently with infrared (IR) measurements [14]. Although embedded TCs can be used to quantitatively investigate the cutting temperature, their applications are generally considered unsatisfactory (since their placement can interfere with heat flow and limit the tool strength), and limited to research in a laboratory setting because of the costly tool insert that requires customized fabrication and the operationally expensive scheduled tool-changes.

As a non-contact alternative, IR thermal imagers (utilizing microbolometer sensitive to infrared light) have been used to measure surface temperature fields for thermal analysis of cutting tool [15] and sheet metal [16] in manufacturing applications. Most existing IR-based measurement devices (that simply use an IR camera quantitative) analyze the data using signal and/or image processing methods [17]. While they are effective to detect certain machining states [18] and can be potentially implemented at low-cost [19], the internal tool temperature field and its peak value (near the tool/chip interface) which are essential information in general machining applications cannot be determined from the measured surface temperature distribution directly. As reported in [20][21][22] where a transparent yittrium aluminum garnet (YAG) tool and a high-resolution IR imager were used, as much as 30% difference between the maximum contact temperature and the maximum surface temperature was experimentally found in orthogonal cutting (with negligible tool-workpiece offset). These findings suggest that a 3D heat transfer model must be coupled with IR measurements to reconstruct the internal temperature field of the cutting tool.

To relax the stringent requirements commonly encountered when using an IR thermal imager for monitoring the internal temperature field during dry cutting, this paper presents a novel dual-field (far-field and near-field) approach for robust feature extraction from IR images and for training ANN with precomputed physics-based models to account for uncertain heat-flux variations at the tool/chip interface. Unlike existing inverse methods solving the PDE with TC-measured temperature, the ANN once trained is computationally efficient [23] and exhibits excellent learning capability in noisy environment with high interpolation accuracy [24]; thus the physics-based ANN could offer a viable easy-to-implement approach in industry. The remainder of this paper offers the followings:

- A 3D conduction heat-transfer model along with the numerical algorithm is formulated for reconstructing the temperature field of the tool from the measured surface temperature field. Based on an order of magnitude analysis, the measured field is divided into a far field and a near field. In the far field, the effect of the frictional tool/chip contact heat on the temperature is treated as an ideal heat-source for solving the heat-transfer coefficient between the tool and ambient temperature. The near field temperature is solved numerically to train an ANN that accounts for the unknown heat-flux variations at the contact interface.
- Practical implementation issues encountered in extracting temperature features that provides the boundary conditions (BCs) for solving the heat transfer equation from the IR surface temperature are discussed. The effects of image resolution, feature selection, chip occlusion, contact heat variation and measurement noises on the maximum contact temperature are analyzed experimentally and numerically using finite-element analysis (FEA). For verification, the ANN-estimated surface temperatures are compared against "true value" experimentally obtained with a high-resolution IR imager on an orthogonal cutting testbed as well as numerical results simulated using FEA.
- The concept-feasibility of the temperature monitoring method based on IR surface temperature measurements and model-trained ANN for online applications is demonstrated on an industrial lathe-turning center. The ANN-estimated results are compared with temperatures experimentally measured using two TCs and a commercial IR imager as well as FEA simulations, which are existing benchmark measurement and numerical methods, commonly reported in published literature. As will be illustrated, this method requires only a small number of pre-selected features from a relatively low-cost standard IR imager (with 320×240 resolution) to reconstruct the internal tool-temperature field, and capable of detecting and substituting any occlusions in the IR images using two thermal properties (isotherms and streamlines). As the method does not rely on expensive close-up lenses to infer the steep temperature gradient near the tool-tip, it represents a practical low-cost solution that has the potential to be utilized in industry.

II. Infrared Image based Temperature monitoring

Fig. 1 illustrates a typical cutting process where frictional heat is generated at the tool/chip contact interface. During machining, the tool insert (with thermal conductivity k, mass density ρ, and specific heat capacity c_p) acts as a heat sink through which the heat flux $q_{s,}$ generated at the tool/chip frictional contact dissipates from its surfaces by convection (characterized by the heat transfer coefficient h that depends on ambient conditions). Mathematically, the steady-state tool temperature T (x, y, z) is governed by the heat conduction equation (1a) where ∇ denotes the gradient operator, which can be uniquely solved with appropriately specified BCs (1b) for a given tool geometry:

$$\nabla(k\nabla T) = 0 \tag{1a}$$

$$\frac{\partial T}{\partial u} = -\frac{1}{k}\begin{cases} q_s(t) & \text{contact area } (u = 0_+) \\ h(T - T_\infty) & \text{far field exposed to ambient} \end{cases} \quad (1b)$$

where $u = x, y$ or z and T_∞ is the ambient temperature. The solutions to (1a, b) for a cutting tool with known material and geometry can be solved if q_s, (and its contact area) and h are specified. In (1b), the **far field** is the region far from the heat source where heat dissipates by convection from the surfaces. The interest here is to monitor the maximum internal temperature T_{im} as well as the maximum surface temperature T_{sm} of the tool during machining, which occur in the **near field** (or the vicinity of the tool/chip interface).

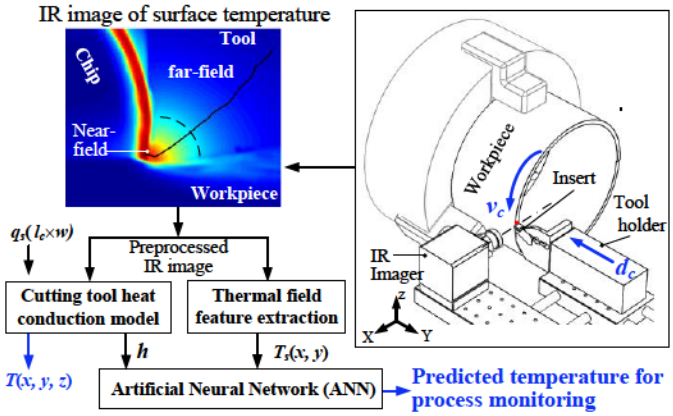

Fig. 1 Cutting temperature measurement system

Unlike material properties, h must be experimentally determined. The contact area (defined here as a product of contact length l_c and cutting thickness w) is generally very small (in microns) relative to the cutting tool, and cannot be measured online. As q_s cannot be measured directly, empirical relationships based on the measured cutting forces are commonly used to approximate q_s that not only depends on specified cutting requirements but also varies with the actual cutting tool conditions. To be effective, the on-line temperature monitoring method has the following abilities:

- It can reconstruct the tool-temperature field around the tool/chip interface and determine its peak value from IR surface temperature measurements.
- It is capable of multi-scale temperature measurements in the micro-scale contact area, and can detect and substitute any chip occlusions during machining.
- It accounts for a range of frictional heat variations at the tool/chip interface.

To meet the above requirements, Fig. 1 illustrates an online method consisting of three parts for monitoring the interface temperature of a cutting tool:

1) an IR imager that moves with the cutting tool for measuring the surface temperature of the tool side;
2) a coupled set of heat transfer models to estimate h and to reconstruct the tool temperature; and
3) a trained artificial neural network (ANN) for on-line monitoring of the tool temperature.

As illustrated in Fig. 1, the on-line method begins with an IR surface temperature image (presented in pseudo-colors for ease of visualization). The fin model described in Appendix, which reduces the processing of a 2D image to that along a streamline and thus speed up the computation, is then used to estimate the heat transfer coefficient h from the far-field temperature. Selected surface temperatures in the near field are extracted as features $T_s(x, y)$ for on-line temperature monitoring of the cutting tool using a trained ANN. For general cutting applications, empirical relationships based on the measured cutting force can be used to approximate q_s along with the on-line estimation of h to specify the boundary conditions in (1b). Once the solutions to (1a, b) are validated, commercial software can be utilized to simulate large data to characterize the 3D temperature field of the cutting-tool, for a range of different (q_s, l_c and h) BCs to support model-based data-driven monitoring of the critical tool temperatures.

A. Physics-based model-trained ANN for online monitoring

Fig. 2 illustrates the method to account frictional heat variations at the tool/chip interface in practice, where the ANN offers a nonlinear mapping between the IR measured surface temperatures (as inputs) and the monitored temperature (as responsive outputs). As shown in Fig. 2(a), large data based on the solutions to (1a) for a specified range of BCs (1b) are computed offline to train an ANN as shown in Fig. 2(b) for model-based monitoring of the critical tool temperature.

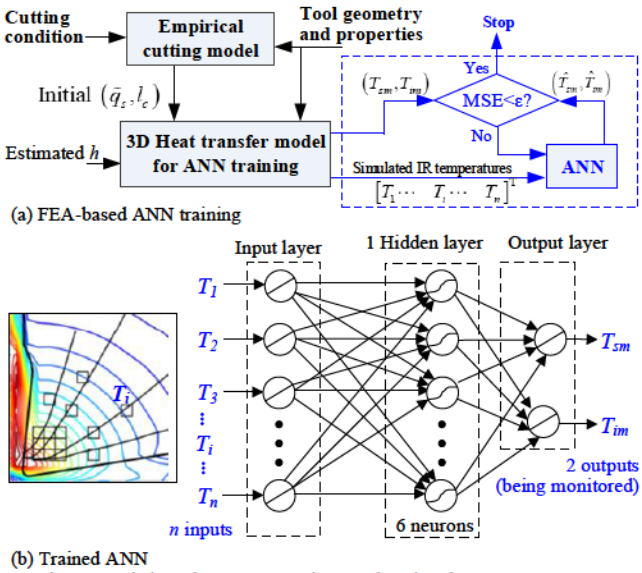

Fig. 2 Training data preparation and trained ANN structure

The off-line training preparation is illustrated in Fig. 2(a) for a given tool and cutting conditions (with constant w), where the initial q_s is estimated empirically. The empirical contact length l_c can be found in [25]. For Ti6Al4V material,

$$l_c = \lambda 1.15 d_c + 0.7 d_c \quad (2)$$

In (2), the chip-compression ratio λ depends on the cutting velocity v_c and depth-of-cut d_c, where the relationship can be found in [25] for a range cutting conditions. The initial q_s is estimated as a fraction of the dissipated heat q_f in terms of the cutting velocity and forces at the tool/chip interface:

$$q_s = \left(\frac{3\beta}{2+3\beta}\right) q_f \text{ where } \beta = \frac{k}{k_w}\sqrt{\frac{\alpha_w}{\alpha_t}} \quad (3a,b)$$

$$\text{and } q_f = v_c\left(f_c \sin\gamma + f_t \cos\gamma\right)/\lambda\,. \quad (3c)$$

In (3b) where (k, α_t) and (k_w, α_w) are the heat conductivity and thermal expansion coefficient of the cutting tool and workpiece materials respectively, the empirical β depends on the materials of the cutting tool and workpiece. In (3c) where γ is the rake angle of the cutting tool, the cutting and feeding forces (f_c, f_t) can be experimentally measured in real time or simulated offline using commercially available cutting software (such as AdvantEdge).

To estimate h in real time, the far-field heat transfer is approximated by a fin model in Appendix where the contact heat is modeled as an ideal point source at $R = 0$ (Fig. A.1); and heat transfer out at the sufficiently far end (at $R = L$) is neglected. The significance of the fin model (A.6) is illustrated with an order-of-magnitude analysis in Appendix, suggesting that the far-field temperature does not depend on φ, and can be determined along a streamline. Thus, the Biot number m (and hence h) can be determined from the isotherms and streamlines of an IR temperature image using (A.6).

Numerically, the temperature fields were found to be more sensitive to q_s than h and l_c. To reduce the number of ANN models (each corresponding to a set of BCs), (h, l_c) are grouped in (p, ℓ) intervals within which their average values $\left(\bar{h}_p, \bar{l}_{c\ell}\right)$ are used:

$$\left(\bar{h}_p, \bar{l}_{c\ell}\right);\ q_{sj} \Rightarrow \left\{\left[T_1 \cdots\ T_i \cdots\ T_n\right]^{\mathrm{T}}, \left[T_{sm}\quad T_{im}\right]^{\mathrm{T}}\right\}_j \tag{4}$$

Since there is no relative motion between the IR imager and the tool, the feature locations are fixed points on the IR images in the ANN where the input-output pairs are defined (4). However, the number of the feature points (that characterize the surface temperatures of the tool insert) and their locations have significant effects on the robustness and accuracy of maximum temperature predicted by the trained ANN.

Once the BCs are completely defined, the 3D temperature field of the cutting tool can be computed from (1a). The ANN is trained with supervised learning using the solutions to (1a) which are solved for a broad range of different boundary conditions (q_s, l_c, h) to generate the input-output data-pairs.

B. Near-field feature extraction with occlusion handling

The IR image provides selected temperature data for the far-field estimation of the heat transfer coefficient h, and for the on-line monitoring of the tool temperature using a trained ANN. In the selection of feature points located in the near field, the assumption of an ideal point heat source is no longer valid. As an illustration, Fig. 3(a) shows an IR image captured during orthogonal cutting and the surface temperature T(s) and its gradient $\partial T/\partial$s along the streamline s. For a homogeneous object, T and $\partial T/\partial s$ are continuous. As defined in its top–right image, the streamline s starts at an arbitrary point where $T(s=0)=T_0$ in far-field, and ends at the tool/chip interface where the temperature is continuous and peaks at $T(s= s_m)=T_m$ but its gradient $\partial T/\partial s$ is discontinuous and equal to 0. To help gain intuitive insights into the heat-source effect on the near-field thermal behaviors, the orthogonal cutting is simulated using FEA in Fig. 3(b) where the top–left plots illustrate the effects of the two heat-sources (same $q_s l_c$ but different l_c) on the isotherms (constant temperature curves) and streamlines (which characterize $\partial T/\partial s$ and are perpendicular to isotherms). In Fig. 3(b) where the (T_0, T_m) values are listed, the temperature difference (T–T_0) is normalized to (T_m–T_0).

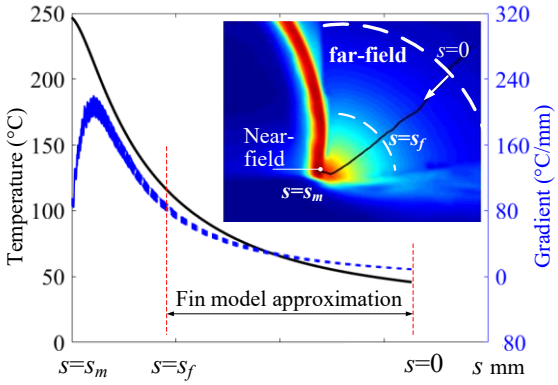

(a) Temperature and its gradient along the streamline

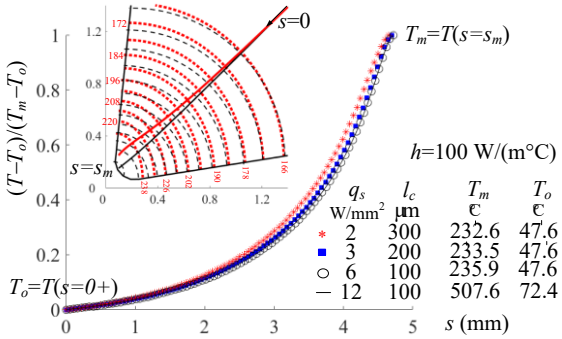

(b) Heat source(q_s,l_c) effect on the normalized temperature distribution

Fig. 3 Temperature along a streamline (near heat source)

The following observations can be made from Fig.3:

- As revealed in the IR image (top-right in Fig. 3a), the $\partial T/\partial s$ monotonically approaches to zero in far field ($0 \le s \le s_f$); and the isotherms are approximately concentric and circular. This is further confirmed in the top-left of Fig. 3(b), where the two streamlines, for l_c=100μm (thin-black line) and for l_c=300μm (red line), converge at far field.
- The near-field temperature and its gradient of the rake surface (top–left in Fig. 3b), depend on the frictional heat-flux q_s and contact length l_c for a given tool geometry (b,φ); see Fig. A.1 in Appendix.
- In Fig. 3(b), the normalized temperature (T–T_0)/(T_m–T_0) along the streamline for a given l_c has the form:

$$\frac{T-T_o}{T_m-T_o} = \exp\left(-\frac{s_m - s}{g}\right) \text{ where } s \ge 0+. \tag{5}$$

  Equation (5) is independent of $q_s l_c$, but weakly depends on l_c as shown in Fig. 3(b).
- For a given $q_s l_c$, l_c has a direct influence on the location of T_m but plays no role in the value of T_m.

In practice, the IR images could be occluded by chips during machining. Thus, the two thermal properties (isotherms and streamlines), which are continuous for a homogeneous object, are used as criteria in the feature selection algorithm to detect and substitute any occlusions in the IR images. The procedure is illustrated numerically with an example in Fig. 4 where a broke-away chip occludes the surface near the tool tip; as a result, the temperature and its gradient are discontinuous along

the streamline, and thus can be detected by the criteria based on the principle of continuity. The temperature values of the occluded pixels can be uncovered using (5) characterized by the two parameters (g, T_m) for a specified streamline (s_o, s_m). As $T(s)$ is extracted while tracing along a streamline, n_s data prior to the occurrence of the occlusion can be used to determine the parameters (g, T_m) for approximating the occluded pixels with (5). The original and replacement temperature along the streamline on the occluded IR image are compared in Fig. 4.

Given that the IR thermal imager is fixed relative to the cutting tool, the feature points for reconstructing the near-field temperature can be pre-selected. To allow for simultaneously uses of the two thermal properties, feature points are selected at intercepts between the streamlines and the isotherms. As will be illustrated experimentally, this scheme significantly improves the robustness of the feature selection in near field.

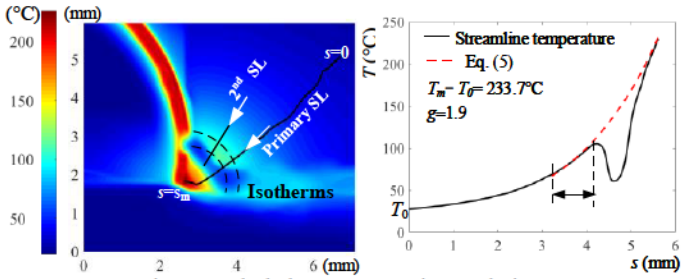

Fig. 4 Occluded temperature interpolation

III. Result and Discussions

The IR-image method with a model-trained ANN for online temperature monitoring of the cutting tool is illustrated and validated numerically and experimentally. Three sets of results are presented: The *first* numerically analyzes the effects of the feature selection and sensor noise on the robustness and accuracy of the model-trained ANN. The *second* investigates the effects of image resolution on the maximum temperature (T_{sm} and T_{im}) estimated by the trained ANN using experimentally obtained IR images. Since no published data were available for benchmark comparison, high-resolution surface-temperatures were obtained both experimentally and numerically in the first two sets of results for investigating the effects of image resolution, temperature gradient and chip occlusion on the online temperature monitoring. Once these effects are well understood, the *third* demonstrates the effectiveness of the model-trained ANN method on an industrial lathe-center with a commercial tool insert, where the surface temperature was measured with a standard IR imager.

The steady-state equation (1a) and its BCs (1b) were numerically solved for the near-field temperature in COMSOL (a commercial 3D FEA software) to simulate the input-output data-pairs for training the ANN shown in Fig. 2(b). The fully connected 3-layer network with a hidden layer of six neurons (sigmoid function) and a pair of input and output layers (linear function) was trained in MATLAB (Neural Network Toolbox) based on the Levenberg-Marquardt algorithm [26].

Experiments were conducted on a customized orthogonal cutting testbed (Fig. 5) [27]with a high-resolution (HR) IR-imager (FLIR A325sc camera with a close-up X1 lens, 320×240 pixels, 60Hz) to allow close capturing of the surface temperature field and its steep gradient around the tool-chip interface. As shown in Fig. 5, the rectangle workpiece was fed vertically with the constant speed towards the high-speed steel (HSS) cutting tool fixed on a stationary tool holder, where the parametric values of the tool are listed in Table 1. The IR imager is mounted (fixed relative to tool table) with its optical axis perpendicular to the side surface of the tool/chip interface of the orthogonal cutting. With this customized setup, the measured surface temperatures (with very high spatial resolution of 25μm/pixel, or in other words, a set of 8×8 measurements within an area of 200μm×200μm) offer the essential 2D "true-values" for experimental verification of the solved temperature field. These data represent an order improvement over the linear distance of 0.2mm (for a single measurement from the tool-tip) reported in [10].

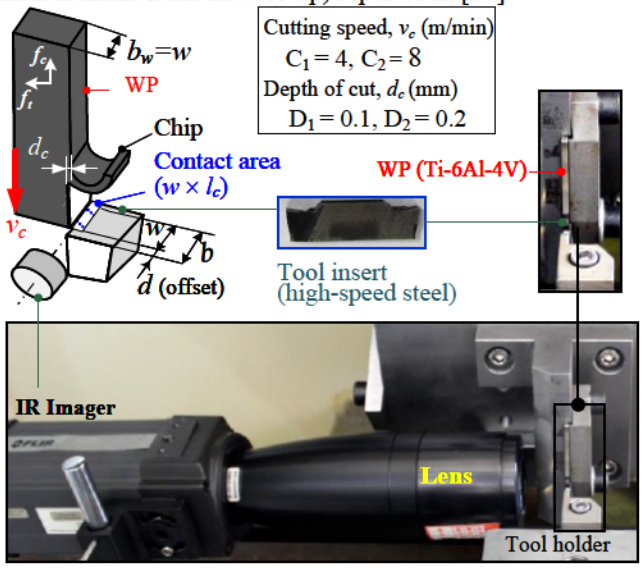

Fig. 5 Experiment with high-resolution IR

Table 1 Parametric values of customized cutting experiments

Materials	ρ (kg/m^3)	c_p (J/kg/ °C)	k (W/m/°C)
WP (Ti4Al6V)	4430	505.6	7
Tool (HSS)	8000	450	15
Tool geometry:	φ =73°, b=2.6mm		
Cutting condition:	v_c =8m/min, d_c =0.2mm		
FEA BCs:	q_s = 6.3W/mm^2; h = 540W/(Km^2); w=2.5mm l_c= 0.3mm		
3,000 training pairs	Initial $\bar{q}_s$ =10.8W/mm^2 and $\bar{l}_c$ = 0.37mm		
	q_s (W/mm^2)	h (W/m^2/℃)	l_c×w (mm^2)
	0.2:0.2:25	100:100:800	0.27,0.54,0.81

In all experiments (T_∞ = 20°C), the workpieces are titanium alloy (Ti-6Al-4V) with characteristic thermal properties given in Table 1. For consistency in IR temperature measurements, a thin-layer of thermal grease (less than 0.5mm thick, k ≈ 1.5W/m/K) with a constant emissivity ε of 0.95 [28] experimentally calibrated using the procedure described in [29] was applied on the viewing surface of the cutting tool, where generally has a high Young's modulus and remains un-deformed during machining.

A. Effects of feature noise and selection on model-trained ANN

Unlike the maximum surface temperature T_{sm} that can be

measured by the high-resolution (HR) imager, the maximum internal temperature T_{im} is hidden and can only be analyzed numerically by solving (1a) with BCs derived from the surface temperature of the side face. For practical implementation on a typical lathe-center that generally does not permit close capturing of the tool/chip interface, the FEA computed temperature is discretized to simulate the spatial resolution commonly in practice. For this reason, the FEA models were coded with high-resolution meshes to provide "numerical true values" for training the ANN, while the simulated surface was discretized to model the low-resolution (LR) of the IR-images in the third set of experiments for comparison.

FEA Models

Fig. 6(a) shows the FEA model (meshed with tetrahedral elements) for the cutting tool in Fig. 5, where most of the elements are located in the region near the tool tip. Table 2 shows the effect of the mesh sizes on the computation errors for maximum and average temperature (relative to Case 6). The numerical study has led to the choice of 104,264 tetrahedral elements with the acceptable computing time of 18 seconds (with the largest element size of 25μm) in the subsequent computation. Fig. 6(b) shows a typical 3D temperature field of the tool, where the parametric values of the cutting condition and the boundary conditions used in the simulation can be found in Table 1. Because of an offset d=0.1mm that was set in the experiment to reduce the chip occlusion in the IR images (Fig. 5), the internal maximum temperature T_{im} is expected to be higher than the surface maximum temperature T_{sm}.

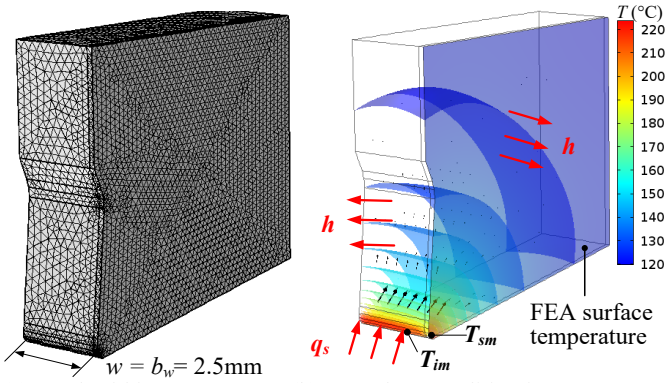

(a) Meshgrid in COMSOL (b) Boundary condition in COMSOL

Fig.6 FEA numerical simulation

Table 2 Effects of mesh numbers on accuracy

Case	Num. of elements	Computing time (seconds)	% Relative Error (Max., Ave.)
1	4,107	6	(21.83, 0.45)
2	15,237	8	(11.06, 0.22)
3	25,441	9	(5.09, 0.12)
4	60,014	14	(1.43, 0.07)
5	104,264	18	(0.37, 0.02)
6	123,654	21	Basis for comparison

With initial $\tilde{q}_s$ =10.8W/mm^2 and $\tilde{l}_c$ =0.37mm computed using (2) and (3), 3000 input-output training pairs over a range of (q_s, h, l_c) as shown in the last row of Table 1 are pre-computed to account any possible variations in BCs during cutting. The ANN weights (Fig. 2b) were trained with 70% of the data-pairs; and the remainder was divided into 2 halves; 15% for validation and 15% for testing. The validation set minimizes overfitting and halt weight updating when the generalization stops improving. The testing set provides an independent measure of the network performance during and after training.

Effect of feature patterns on model-trained ANN

The number of feature points and their locations (which are referred to here as feature patterns) have significant effects on the robustness and accuracy of the trained ANN as well as on the computation time required to train the ANN and the online recall. The time required to train the ANN with 750 data pairs (on a 64-bit PC, Intel Core i7-6600, 2.6GHz,16GB RAM) is 25.75 minutes when all 403 points in a original temperature distribution image are treated as features, which would be 5.1 minutes for training with 20 feature points and 3.75 minutes for 15 feature points. With no detection of image occlusion, the ANN takes 8.3ms (referred to here as recall time) to estimate two outputs (T_{sm}, T_{im}) with 20 inputs, and 5.5ms with 15 inputs. As an illustration, Fig. 7(a) compares three different types of 15-point-distribution in the simulated image:

D1: 3 streamlines, each with 5 equally spaced points.

D2: Similar to D1 but points distributed using the bisection method to account the increasing gradient in the near field.

D3: 9 equally spaced points in near field and 6 other points at intercepts between the streamlines and isotherms.

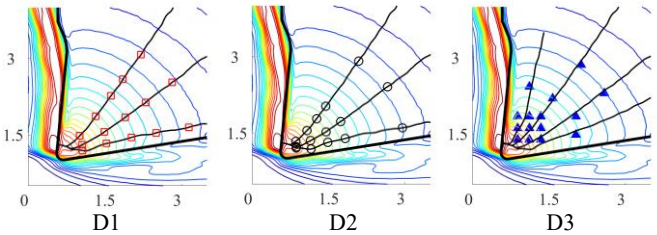

(a) Three different feature point distribution of 15 points

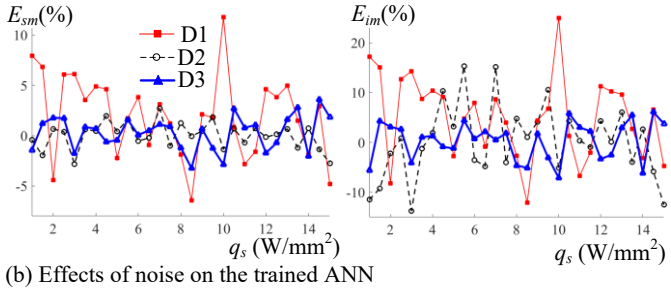

(b) Effects of noise on the trained ANN

Fig. 7 Feature points selection and analysis

To investigate the effects of the feature pattern on the robustness, a random zero-mean (μ=0) Gaussian noise to the FEA-simulated input T_i so that the feature surface temperatures ($\tilde{T}_i$ where i= 1, ..., n) are numerically corrupted by noise, and have the form in (6) where ε_i is the random error associated with the i^{th} measurement and σ is a standard deviation:

$$\tilde{T}_i = T_i + \varepsilon_i(\mu, \sigma) \tag{6}$$

Fig. 7(b) compares the effects of the corrupted inputs (σ= $0.05T_i$) on the robustness (among three types of distribution) in terms of the errors (E_{sm} and E_{im}) defined in (7):

$$E_m(\%) = 100\left(\tilde{T}_m - T_m\right)/T_m \tag{7}$$

In (7), ($\tilde{T}_{sm}$ and $\tilde{T}_{im}$) are the outputs of the trained ANN in response to the noise-corrupted inputs, and (T_{sm} and T_{im}) are the "true-value" originally computed by the FEA. For the equally spaced D1, the maximum (E_{sm}, E_{im}) values are (12%, 25%) which can be effectively reduced to (4%, 15%) for D2 and (4.5%, 7%) for D3 as numerically demonstrated in Fig. 8(b).

B. Effect of image resolution on model-trained ANN

To investigate the effect of image resolution on the trained ANN, HR (25μm/pixel) images were captured on the customized orthogonal cutting setup (Fig. 5), from which LR images (with a 10× scaled down to simulate the resolution of 250μm/pixel typically found in surface temperature measurements of a standard IR imager) were obtained. The HR and LR IR-images are compared in Fig. 8(a). The 15-feature D3 scheme was experimentally evaluated on the IR images for four cutting conditions (C_i, D_i) where the subscripts (i=1, 2) of the cutting speed v_c (m/min) and the depth-of-cut d_c (mm) are defined in Fig. 5:

CC1 (4, 0.2); **CC2 (8, 0.2)**; CC3 (4, 0.1); CC4 (8, 0.1)

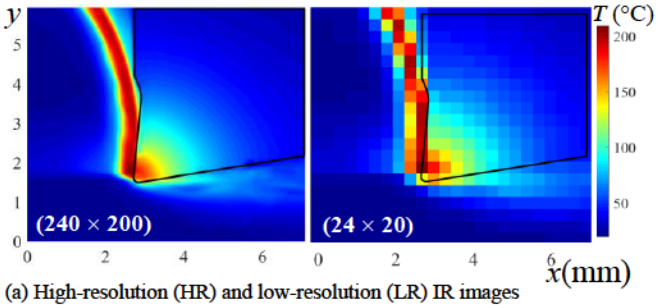

(a) High-resolution (HR) and low-resolution (LR) IR images

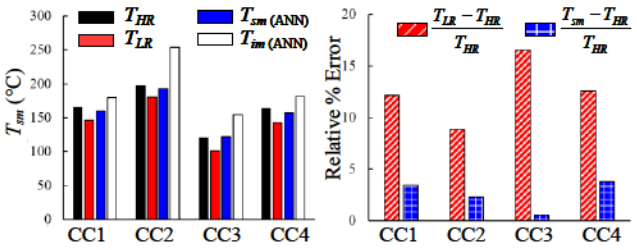

(b) ANN estimated T_{sm} and relative errors

Fig. 8 Results of maximum machining temperature prediction

Some findings from Fig. 8 are summarized as follows:

- As each LR pixel-value represents an average value over 10×10 HR pixels, the LR measured T_{sm} values are lower than and thus underestimate the "true value" (HR measurements). The maximum relative errors in these four experimental cutting conditions are in the order of 15%.
- The T_{sm} error caused by the low-resolution of the IR imager can be effectively reduced by the model-trained ANN. As shown in Fig. 8(b), the error of the ANN-estimated T_{sm} is reduced to less than 5% of the "true value", which represents an order-of-magnitude improvement over the measurements with the LR imager.
- Additionally, the model-trained ANN offers a means to determine the maximum temperature T_{im} in the tool/chip interface, which cannot be captured by IR due to the small offset d=0.1mm between the tool and workpiece.

The effects of low image resolution on a feature pattern is illustrated in Fig. 9(a), where 6 different patterns in a FEA simulated image (12×12pixels, 250μm/pixel resolution) are compared; 5 features in P1, 9 in P2, 15 in each of the P3, P4 and P5 patterns, and 20 features in P6. To predict the effects of low image resolution on the robustness, the model-trained ANN is recalled with and without Gaussian noise as defined in (6). Fig. (9b) comparing the (T_{sm} and T_{im}) errors defined in (7) in terms of noise (varying from 0.1% to 5% of T_i) among the six input-patterns, where each error represents an average over 30 different q_s (with constant l_c and h).

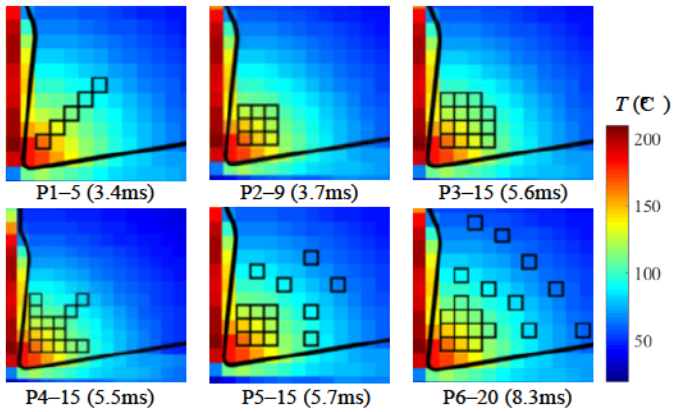

(a) Feature pattern in a 3mm×3mm image, P1 to P6 (recall time)

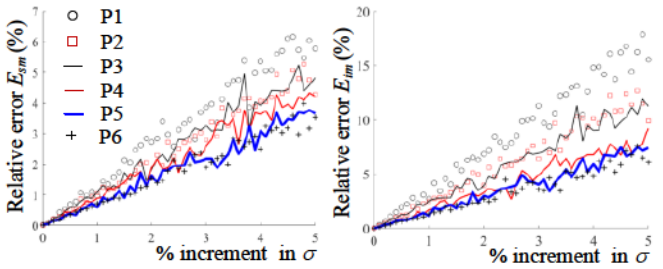

(b) Effects of measurement noise on T_{sm} and T_{im}

Fig. 9 Feature points selection and analysis

Without noise, the model-trained ANN is capable of estimating (T_{sm} and T_{im}) from the low-resolution surface temperature measurements with a mean relative error of less than 0.1%. As the signal-to-noise ratio degrades (Fig. 9b), the estimation becomes less accurate but can be improved by increasing the number of feature inputs. As shown in Fig. 9(b), T_{sm} can be estimated with less than 5% errors from 15 low resolution measurements; and the T_{im} estimation errors were reduced from 17% (P1 with 5 feature inputs) to less than 10% (P3, P4 with 15 feature inputs). Significant improvements can be further achieved by appropriately distributing the 15 features (P5) cover both the far field and near field and located on the intercepts (between isotherms and streamlines), reducing the relative (T_{sm} and T_{im}) errors to (3%, 5%). Further increasing in the feature inputs to 20 at the expense of online recall time does not significantly improve the robustness. Thus, the feature pattern P5 is chosen in the subsequent experiments.

C. Experimental validation

The online monitoring method using surface temperature measurements with a model-trained ANN was evaluated on a conventional lathe center with a commercial tool insert for high-speed orthogonal cutting of a titanium workpiece (Fig. 10),

where the tool geometry is relatively more complex than that in the customized setup (Fig. 5). The surface temperature was measured by the FLUKE Ti400 IR imager (250μm/pixel resolution and 9Hz frame-rate). Due to the limited image resolution, the IR observed maximum is lower than the actual tool maximum temperature during machining. To validate the FEA-computed internal temperature experimentally, the two thermocouples are embedded 0.5mm and 1mm from the tool tip to measure the temperature in real time.

The parametric values of the cutting condition, the BCs for FEA and the number of data-pairs for training ANN in this experimental evaluation are summarized in Table 3. The results obtained experimentally are summarized in Figs. 11 and 12, and Table 4.

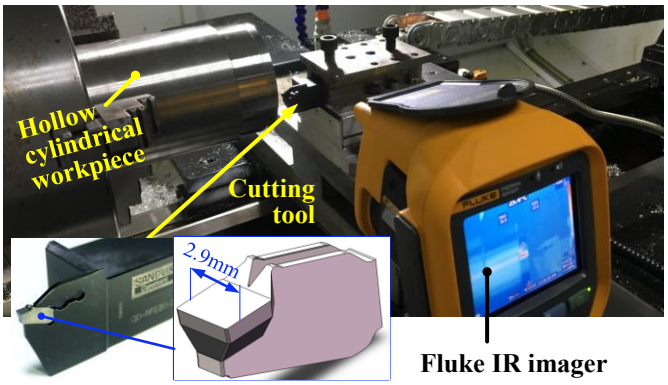

Fig. 10 Experimental setup

Table 3 Parametric values of the lathe-turning center

Materials	ρ (kg/m^3)	c_p (J/kg/ °C)	k (W/m/°C)
Tool (WC/Co)	14000	148	55
Tool geometry:	φ =79°, b=2.9mm		
Cutting condition:	v_c =120.2m/min, d_c =0.1mm		
BCs:	q_s = 54.5W/mm^2; h = 512W/(Km^2); w=1.5mm l_c= 0.17mm		
3,000 training pairs	Initial $\bar{q}_s$ =124.6W/mm^2 and $\bar{l}_c$ = 0.185mm		
	q_s (W/mm^2)	h (W/m^2/℃)	$l_c \times w$ (mm^2)
	2:2:250	100:100:800	0.255

Fig. 11(a) shows the FEA model (meshed with 699,204 tetrahedral elements in COMSOL) of the cutting tool-insert to solve for the temperature field, where the two thermocouples TC1 and TC2 embedded in the tool-insert capable of transient measurements. The time dependent term, $\rho c_p(\partial T/\partial t)$, was included on the right side of (1a) to solve for the 3D transient temperature in FEA. Fig. 11(b) shows a typical IR surface and the following four different feature patterns as real-time inputs to the model-trained ANN.

Case 1: Same as D2 in Fig. 7(a)

Cases 2, 3, 4: Same as (P3, P4, P5) in Fig. 9 respectively.
Case 4a) with no detection of image occlusion
Case 4b) with online detection of image occlusion

The effects of the four feature patterns (all with 15 feature points) on the maximum surface and internal temperatures monitored in real time were experimentally evaluated. For each feature pattern, the three-layer ANN (15 inputs, 6 hidden-neurons and 2 outputs) take less than 4 minutes to complete the offline training. Table 4 tabulates the time required for online data-recall time in milliseconds (ms), the average (Ave.), standard deviations (SD) and maximum (Max.) errors of the ANN-estimated T_{sm} and T_{im}, where the errors are relative to that computed by the FEA. The online recall with no detection of image occlusion (Cases 1, 2, 3 and 4a) took less than 6ms. In Case 4b (where any discontinuities due to image occlusion were detected online), the ANN took 12.1ms to compute the outputs but greatly improve the T_{im} estimation.

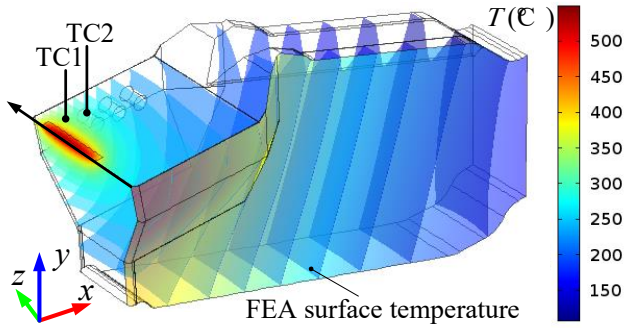

(a) 3D temperature distribution by FEA

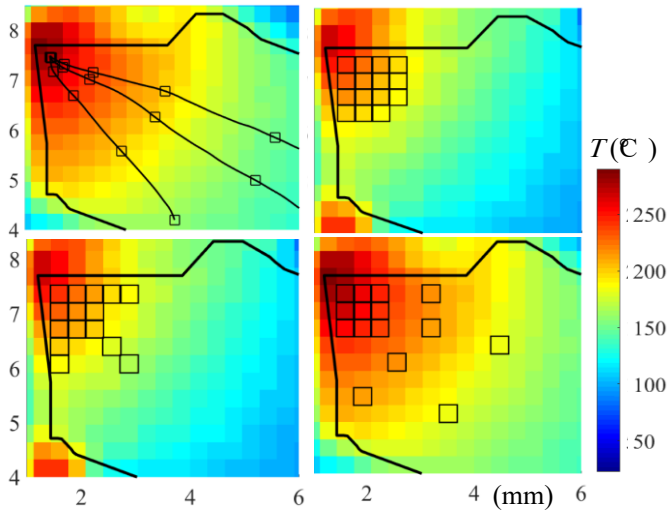

(b) Feature points in IR image

Fig. 11 Training pairs and feature points

Table 4 Comparison of monitoring results

$E = (\lvert T_{ANN} - T_{FEA} \rvert) / T_{FEA}$ **(Ave., SD, Max.)**			**Recall (ms)**
Pattern	E_{sm}	E_{im}	
Case 1	(1.9, 1.8, 7.7)	(8.3, 5.4, 25.3)	5.4
Case 2	(9.3, 3.1, 18.3)	(15.6, 10.1, 44.2)	5.6
Case 3	(3.2, 2.1, 10.4)	(9.5, 6.1, 22.5)	5.5
Case 4a	(2.1, 1.2, 4.8)	(7.4, 5.3, 21.3)	5.7
Case 4b	(2.1, 0.96, 4.1)	(2.7, 3.5, 10.9)	12.1

Using the feature pattern in Case 4b (Fig. 11) as ANN inputs, the effectiveness of the FEA, online image-occlusion detection, and model trained ANN were experimentally validated. The results are illustrated in Figs. 12(a, b, c) Fig. 12(a) shows a typical image captured during transient, within which the distinct edge lines are detected by the local changes in intensity of IR image. Based on the edge lines of the tool insert (green lines in the middle of Fig. 12a), where the tool outline was

determined online by means of a pattern-matching algorithm with known tool geometry. As shown in Fig. 12(a), the tool/chip interface is in the scale of microns.

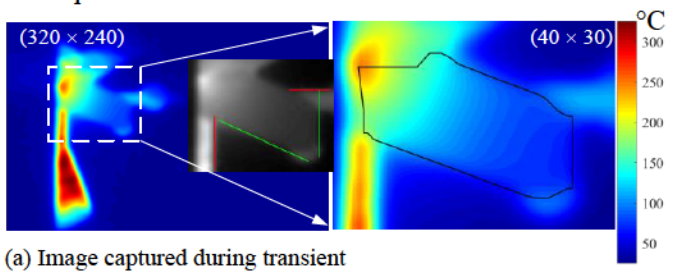

(a) Image captured during transient

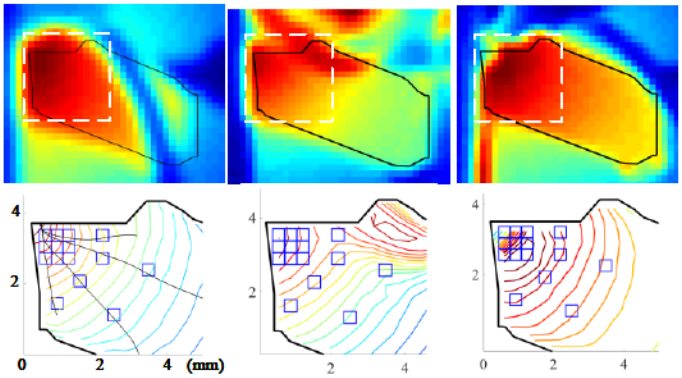

(b) Chip occlusion during monitoring

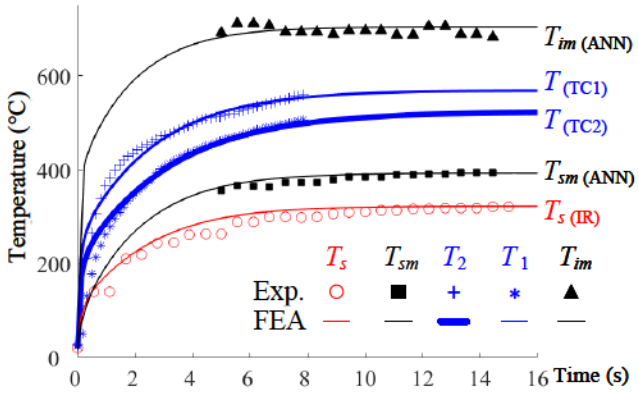

(c) Comparison among FEA, ANN and measurements

Fig. 12 Experimental investigation on conventional lathe center

Three examples are given in Fig. 12(b) to illustrate image occlusion and its handling for obtaining high fidelity surface temperature features as inputs to the trained ANN:

- The *first* column shows a breakaway chip occluding the image in the far-field region. As h does not change significantly between time steps, the value of h from the previous time-step is assumed. The non-occluded feature temperatures are inputs to ANN for estimating the target output temperatures being monitored.
- The *second* column shows a sweeping chip occluding a portion of feature temperatures in the far field at the steady state. The occlusion was detected, where drastic temperature differences between the points on the same isotherm and between two consecutive time steps occur. The occluded temperatures were then replaced by a value interpolated from the non-occluded feature temperatures.
- The *third* column shows a chip in near field, which was detected as it exhibits a dramatic temperature-discontinuity with other feature temperatures on a specific isotherm. Using the streamlines in the near field, the occluded temperatures are replaced with interpolated values computed from the exponential fit illustrated in (5).

With the high-fidelity feature-inputs, the temperatures (T_{sm} and T_{im}) being monitored online can be estimated from the ANN trained with FEA models. Fig. 12(c) plots the FEA-simulated temperatures at specified locations during transient and steady state, which are compared with measurements using the proposed and existing benchmark measurement methods. Specifically, the FEA results are compared against the IR-measured surface temperature T_s (discrete red circle) at an observed point, the ANN-estimated T_{sm} and T_{im} (discrete black square and triangle respectively), and the thermocouple measurements (TC1 and TC2) during cutting. Although the IR imager is capable of measuring the surface temperature during transient, the ANN was trained with surface temperature measurements at steady state; thus, only the steady state (ANN-estimated) T_{sm} and T_{im} are plotted in Fig. 12(c). The followings are some observations made in the comparisons:

- Because of the limited IR-image resolution, the observed maximum surface temperature underestimates the actual maximum temperature of the cutting tool. The TC1 and TC2 measurements (located at 0.5 and 1mm apart from the tool tip) support the need for a model-trained method.
- Since T_{im} cannot be experimentally measured, the FEA simulates the transient response so that the FEA model (and hence the model-trained ANN) can be validated by comparing with TC1, TC2 and T_s measurements at the specified positions. The good agreement among the FEA, the ANN estimation, thermocouple measurements, and IR surface temperatures confirm the effectiveness of the model-trained ANN in practical dry-cutting environment.

IV. Conclusion

An online temperature monitoring system consisting of an IR thermal imager, far-field and near-field heat transfer models, and a model-trained ANN for monitoring the maximum steady-state temperature at the tool/chip interface during dry cutting has been presented. The IR image provides selected temperature feature points for estimating the heat transfer coefficient h, and for on-line monitoring of the tool temperature using a trained ANN. The robustness of the ANN-estimated surface temperatures has been verified against data from a high-resolution IR imager (with a 10×10 higher spatial resolution than typical standard IR imager) as well as numerically simulated using FEA.

Experimentally investigated on a lathe-turning center with a commercial tool-insert that has a relatively more complex geometry, the robustness of the near-field temperature reconstruction can be significantly improved with pre-selected intercepts between the streamlines and the isotherms as feature points. With 15 points, the three-layer ANN (15 inputs, 6 hidden-neurons and 2 outputs) took less than 4 minutes to complete the offline training, and 12.1ms to recall (T_{sm}, T_{im}) which includes the time to detect any discontinuities due to image occlusion. For each feature pattern, the average, standard

deviation and maximum errors of the ANN-estimated T_{sm} and T_{im} relative to that computed by the FEA are (2.1%, 0.96%, 4.1%) and (2.7%, 3.5%, 10.9%) respectively.

The ANN-estimated results agree well with the temperatures measured with two built-in TCs and commercial IR imager as well as FEA simulations. Results show that the steady-state maximum temperature at the tool/chip interface was 620°C as compared to the maximum surface temperature of 320°C directly measured by the IR imager.

APPENDIX
FIN MODEL

Figure A.1 shows a tool-insert (characterized by the geometric parameters, thickness b and angle φ) modeled in cylindrical coordinates for estimating the heat transfer coefficient h. Because of the high thermal conductivity and small thickness of the tool insert, (1a) is approximated by the following fin model:

$$\frac{\partial}{\partial r}\left[k(T)A(r)\frac{\partial T(r)}{\partial r}\right]-h(T)\frac{d[a(r)]}{dr}[T(r)-T_\infty]=0 \qquad \text{(A.1)}$$

In (A.2) where r is the radial distance from the tool tip, the 1st term accounts for heat conduction through the cross-section area $A(r)$ whereas the 2nd term models the heat convection at the cooling surface area $a(r)$:

$$A(r)=b\varphi r \text{ and } a(r)=\varphi r^2+2rb\,. \qquad \text{(A.2a,b)}$$

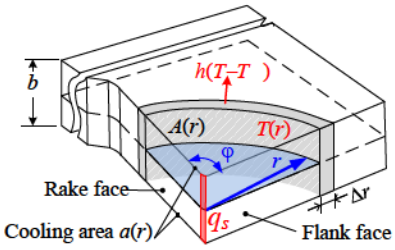

Fig. A.1 Fin model in cylindrical coordinates

For generality, the following dimensionless parameters (θ, R, L, Q_s) are used to normalize the governing equations:

$$\frac{(T_m-T_\infty)\theta}{T-T_\infty}=\frac{R}{r/b}=\frac{L}{l/b}=\frac{kT_\infty Q_s}{bq_s}=1 \qquad \text{(A.3a~d)}$$

Consider a steady state (with uniform k and h) leading to a Sturm-Liouville problem (A.4a) where m^2 is the Biot number and the BCs (A.4c, d):

$$R\frac{d^2\theta}{dR^2}+\frac{d\theta}{dR}-\frac{m^2}{\varphi}(R\varphi+1)\theta=0 \text{ where } m^2=\frac{2hb}{k} \qquad \text{(A.4a,b)}$$

$$\left.\frac{d\theta}{dR}\right|_{R=0}=Q_s \text{ and } \left.\frac{d\theta}{dR}\right|_{R=L}=0\,. \qquad \text{(A.4c,d)}$$

For a large R such that $R\varphi >> 1$,

$$\frac{d^2\theta}{dR^2}-m^2\theta=0 \qquad \text{(A.5)}$$

Along with the BCs (A. 4c,d), the solution to (A.5) is given by

$$\frac{\theta}{\theta_c}=\frac{-\cosh m(L-R)}{\sinh mL} \text{ where } \theta_c=\frac{Q_s}{m} \qquad \text{(A.6)}$$

ACKNOWLEDGMENT

The authors sincerely thank Dr. Xiaoming Zhang, Mr. Dong Zhang, Dr. Zhenhua Xiong and Dr. Haifeng Ma for their helps with the CNC turning center and measuring equipment.

REFERENCES

[1] Y. Cheng and M. A. Jafari, "Vision-based online process control in manufacturing applications," *IEEE Trans. Autom. Sci. Eng.*, vol. 5, no. 1, pp. 140–153, 2008.

[2] K. Liu, X. Zhang, and J. Shi, "Adaptive sensor allocation strategy for process monitoring and diagnosis in a Bayesian network," *IEEE Trans. Autom. Sci. Eng.*, vol. 11, no. 2, pp. 452–462, 2014.

[3] S. A. Vaghefi, M. A. Jafari, J. Zhu, J. Brouwer, and Y. Lu, "A Hybrid Physics-Based and Data Driven Approach to Optimal Control of Building Cooling/Heating Systems," *IEEE Trans. Autom. Sci. Eng.*, vol. 13, no. 2, pp. 600–610, 2016.

[4] Y. Zhang, Y. Fan, and W. Du, "Nonlinear Process Monitoring Using Regression and Reconstruction Method," *IEEE Trans. Autom. Sci. Eng.*, vol. 13, no. 3, pp. 1343–1354, 2016.

[5] N. A. Abukhshim, P. T. Mativenga, and M. A. Sheikh, "Heat generation and temperature prediction in metal cutting : A review and implications for high speed machining," *Int. J. Mach. Tools Manuf.*, vol. 46, pp. 782–800, 2006.

[6] S. R. Carvalho, S. M. M. Lima e Silva, A. R. Machado, and G. Guimarães, "Temperature determination at the chip-tool interface using an inverse thermal model considering the tool and tool holder," *J. Mater. Process. Technol.*, vol. 179, no. 1–3, pp. 97–104, 2006.

[7] Y. Sun, J. Sun, J. Li and Q. Xiong, "An experimental investigation of the influence of cutting parameters on cutting temperature in milling Ti6Al4V by applying semi-artificial thermocouple", *The Int. J. of Adv. Manuf. Tech.*, vol. 70, no. 5, pp. 765-773, 2014.

[8] D. Werschmoeller, K. Ehmann, and X. Li, "Tool embedded thin film microsensors for monitoring thermal phenomena at tool-workpiece interface during machining," *J. Manuf. Sci. Eng.*, vol. 133, no. 2, p. 21007, 2011.

[9] D. Werschmoeller, X. Li, and K. Ehmann, "Measurement of transient tool-internal temperature fields during hard turning by insert-embedded thin film sensors," *J. Manuf. Sci. Eng.*, vol. 134, no. 6, p. 61004, 2012.

[10] L. Li, B. Li, K. F. Ehmann, and X. Li, "A thermo-mechanical model of dry orthogonal cutting and its experimental validation through embedded micro-scale thin film thermocouple arrays in PCBN tooling," *Int. J. Mach. Tools Manuf.*, vol. 70, pp. 70–87, 2013.

[11] J. Ji, Y. Huang and K.-M. Lee, "A hybrid method based on macro-micro modeling and infrared imaging for tool temperature reconstruction in dry turning," *IEEE/ASME Trans. on Mechatronics* DOI 10.1109/TMECH.2017.2731803. Published online: 25 July 2017.

[12] B. H. S. Atlati and M. N. M. Zenasni, "Analysis of the heat transfer at the tool – workpiece interface in machining: determination of heat generation and heat transfer coefficients," *Heat Mass Transf.*, vol. 51, no. 10, pp. 1355–1370, 2015.

[13] L. Liang, H. Xu, and Z. Y. Ke, "An improved three-dimensional inverse heat conduction procedure to determine the tool-chip interface temperature in dry turning," *Int. J. Therm. Sci.*, vol. 64, pp. 152–161, 2013.

[14] B. S. Prasad, K. A. Prabha, and P. V. S. G. Kumar, "Condition monitoring of turning process using infrared thermography technique – An experimental approach," *Infrared Phys. Technol.*, vol. 81, no. March, pp. 137–147, 2017.

[15] C. Dinc, I. Lazoglu, and A. Serpenguzel, "Analysis of thermal fields in orthogonal machining with infrared imaging," *J. Mater. Process. Technol.*, vol. 198, no. 1–3, pp. 147–154, 2008.

[16] Y.-M. H. Ng, M. Yu, Y. Huang, and R. Du, "Diagnosis of sheet metal stamping processes based on 3-D thermal energy distribution," *IEEE Trans. Autom. Sci. Eng.*, vol. 4, no. 1, pp. 22–30, 2007.

[17] S. Bagavathiappan, B. B. Lahiri, T. Saravanan, J. Philip, and T. Jayakumar, "Infrared thermography for condition monitoring - A review," *Infrared Phys. Technol.*, vol. 60, pp. 35–55, 2013.

[18] M. Elgargni, A. Al-Habaibeh, and A. Lotfi, "Cutting tool tracking and recognition based on infrared and visual imaging systems using

principal component analysis (PCA) and discrete wavelet transform (DWT) combined with neural networks," *Int. J. Adv. Manuf. Technol.*, vol. 77, no. 9–12, pp. 1965–1978, 2015.

[19] A. Al-Habaibeh and R. Parkin, "An autonomous low-cost infrared system for the on-line monitoring of manufacturing processes using novelty detection," *Int. J. Adv. Manuf. Technol.*, vol. 22, no. 3–4, pp. 249–258, 2003.

[20] J. C. Heigel, E. Whitenton, B. Lane, M. A. Donmez, V. Madhavan, and W. Moscoso-Kingsley, "Infrared measurement of the temperature at the tool-chip interface while machining Ti-6Al-4V," *J. Mater. Process. Technol.*, vol. 243, pp. 123–130, 2016.

[21] D. Soler, T. H. C. Childs, and P. J. Arrazola, "A note on interpreting tool temperature measurements from thermography," *Mach. Sci. Technol.*, vol. 19, no. 1, pp. 174–181, Jan. 2015.

[22] P.-J. Arrazola, P. Aristimuno, D. Soler, and T. Childs, "Metal cutting experiments and modelling for improved determination of chip/tool contact temperature by infrared thermography," *CIRP Ann. - Manuf. Technol.*, vol. 64, no. 1, pp. 57–60, 2015.

[23] S. Deng and Y. Hwang, "Applying neural networks to the solution of forward and inverse heat conduction problems," *Int. J. Heat Mass Transf.*, vol. 49, no. 25–26, pp. 4732–4750, 2006.

[24] B. Yuce and Y. Rezgui, "An ANN-GA Semantic Rule-Based System to Reduce the Gap Between Predicted and Actual Energy Consumption in Buildings," *IEEE Trans. Autom. Sci. Eng.*, vol. 14, no. 3, pp. 1351–1363, 2017.

[25] S. A. Iqbal, P. T. Mativenga, and M. A. Sheikh, "A comparative study of the tool-chip contact length in turning of two engineering alloys for a wide range of cutting speeds," *Int. J. Adv. Manuf. Technol.*, vol. 42, no. 1–2, pp. 30–40, 2009.

[26] D. W. Marquardt, "An algorithm for least squares estimation of non-linear parameters," *J. Soc. Ind. Appl. Math.*, vol. 11, no. 2, pp. 431–441, 1963.

[27] D. Zhang, X.-M. Zhang, W.-J. Xu, and H. Ding, "Stress field analysis in orthogonal cutting process using digital image correlation technique," *J. Manuf. Sci. Eng.*, vol. 139, no. 3, pp. 31001–13, 2016.

[28] J. Ji, K.-M. Lee, C.-Y. Lin, and Y. Huang, "An Investigation on temperature measurements for machining of titanium alloy using ir imager with physics-based reconstruction," *Proc. of IEEE/ASME Int. Conf. on Adv. Intell. Mechatronics*, Busan, Korea, July 8-12, 2015.

[29] J. Ji, Y. Huang, and K.-M. Lee, "Cutting tool temperature field reconstruction using hybrid macro/micro scale modeling for machining of titanium alloy," *Proc. of IEEE/ASME Int. Conf. on Adv. Intell. Mechatronics(AIM)*, Banff, Canada, July 12-15, 2016.

Kok-Meng Lee (M'89–SM'02–F'05) received the B.S. degree in mechanical engineering from the State University of New York, Buffalo, NY, USA, in 1980, and the S.M. and Ph.D. degrees in mechanical engineering from the Massachusetts Institute of Technology, Cambridge, MA, USA, in 1982 and 1985, respectively.

He is currently a Professor with the George W. Woodruff School of Mechanical Engineering, Georgia Institute of Technology, Atlanta, GA, USA. He is also a Distinguished Professor with the State Key Laboratory of Digital Manufacturing Equipment and Technology, Huazhong University of Science and Technology, Wuhan, China, under the National Recruitment Program of Global Experts. His research interests include system dynamics/control, robotics, automation, and mechatronics. He holds eight patents in machine vision, three degrees-of-freedom spherical motor/encoder, and live-bird handling system.

Dr. Lee is a fellow of the American Society of Mechanical Engineers (ASME). He received the National Science Foundation Presidential Young Investigator, the Sigma Xi Junior Faculty Research, the International Hall of Fame New Technology, and the Kayamori Best Paper Awards. He was also honored as a Pao Yu-Kong Chair Professor at Zhejiang University, Hangzhou, China.

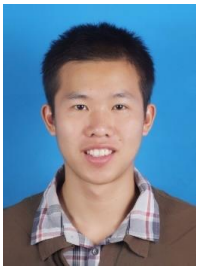

Yang Huang received the B.S. degree in material processing engineering from Huazhong University of Science and Technology, Wuhan, China, in 2013.

He is currently working toward the Ph.D. degree in mechanical engineering at Huazhong University of Science and Technology, Wuhan, China. He was a visiting scholar at George W. Woodruff School of Mechanical Engineering, Georgia Institute of Technology, Atlanta, GA, USA, during 2016-2017. His research interests include mechatronics in manufacturing, thermal field reconstruction, and machining process modeling.

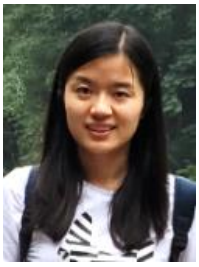

Jingjing Ji (M'14) received the B.S. and Ph.D. degrees in mechanical engineering from Zhejiang University, Hangzhou, China, in 2008 and 2014, respectively.

She was a visiting scholar in Georgia Institute of Technology, Atlanta, GA, USA, during 2012-2013. She is currently an Associate Professor with the State Key Laboratory of Digital Manufacturing Equipment and Technology, School of Mechanical Science and Engineering, Huazhong University of Science and Technology, Wuhan, China. Her research interests include mechatronics, robotics, design, modeling and field reconstruction.

Chun-Yeon Lin received the B.S. degree in mechanical engineering from National Central University, Taiwan. in 2003, the M.S. degree in electrical control engineering from National Chiao-Tung University, Taiwan, in 2005, the M. S. degree in mechanical engineering from Stanford University, Stanford, CA, USA in 2011, and the Ph.D. degree in mechanical engineering from the George W. Woodruff School of mechanical engineering, Georgia Institute of Technology, Atlanta, GA, USA, in 2017.

His current research interests include mechatronics, physical field modeling, machine vision and intelligent systems.